







Article

Near-Infrared (NIR) Silver Sulfide (Ag₂S) Semiconductor Photocatalyst Film for Degradation of Methylene Blue Solution

Zahrah Ramadlan Mubarakah ¹, Norsuria Mahmed ^{1,2,*}, Mohd Natashah Norizan ^{2,3} , Ili Salwani Mohamad ^{2,3} , Mohd Mustafa Al Bakri Abdullah ^{1,2}, Katarzyna Bloch ⁴, Marcin Nabiałek ⁴ , Madalina Simona Baltatu ^{5,*} , Andrei Victor Sandu ^{5,6,7}  and Petrica Vizureanu ^{5,8} 

- ¹ Faculty of Chemical Engineering & Technology, Universiti Malaysia Perlis (UniMAP), Arau 01000, Malaysia
 - ² Centre of Excellence Geopolymer and Green Technology (CEGeoGTech), Universiti Malaysia Perlis (UniMAP), Arau 01000, Malaysia
 - ³ Faculty of Electronic Engineering & Technology, Universiti Malaysia Perlis (UniMAP), Arau 02600, Malaysia
 - ⁴ Faculty of Mechanical Engineering and Computer Science, Częstochowa University of Technology, 42-201 Częstochowa, Poland
 - ⁵ Department of Technologies and Equipments for Materials Processing, Faculty of Materials Science and Engineering, Gheorghe Asachi Technical University of Iași, Blvd. Mangeron, No. 51, 700050 Iași, Romania
 - ⁶ National Institute for Research and Development in Environmental Protection INCDFPM, Splaiul Independentei 294, 060031 Bucharest, Romania
 - ⁷ Romanian Inventors Forum, Str. Sf. P. Movila 3, 700089 Iași, Romania
 - ⁸ Technical Sciences Academy of Romania, Dacia Blvd 26, 030167 Bucharest, Romania
- * Correspondence: norsuria@unimap.edu.my (N.M.); cercel.msmona@yahoo.com (M.S.B.)

Abstract: A silver sulfide (Ag₂S) semiconductor photocatalyst film has been successfully synthesized using a solution casting method. To produce the photocatalyst films, two types of Ag₂S powder were used: a commercialized and synthesized powder. For the commercialized powder (CF/comAg₂S), the Ag₂S underwent a rarefaction process to reduce its crystallite size from 52 nm to 10 nm, followed by incorporation into microcrystalline cellulose using a solution casting method under the presence of an alkaline/urea solution. A similar process was applied to the synthesized Ag₂S powder (CF/syntAg₂S), resulting from the co-precipitation process of silver nitrate (AgNO₃) and thiourea. The prepared photocatalyst films and their photocatalytic efficiency were characterized by Fourier transform infrared spectroscopy (FTIR), X-ray diffraction (XRD), and UV-visible spectroscopy (UV-Vis). The results showed that the incorporation of the Ag₂S powder into the cellulose films could reduce the peak intensity of the oxygen-containing functional group, which indicated the formation of a composite film. The study of the crystal structure confirmed that all of the as-prepared samples featured a monoclinic acanthite Ag₂S structure with space group P₂₁/C. It was found that the degradation rate of the methylene blue dye reached 100% within 2 h under sunlight exposure when using CF/comAg₂S and 98.6% for the CF/syntAg₂S photocatalyst film, and only 48.1% for the bare Ag₂S powder. For the non-exposure sunlight samples, the degradation rate of only 33–35% indicated the importance of the semiconductor near-infrared (NIR) Ag₂S photocatalyst used.

Keywords: near-infrared irradiation; silver sulfide; cellulose film; photocatalysis; methylene blue



Citation: Mubarakah, Z.R.; Mahmed, N.; Norizan, M.N.; Mohamad, I.S.; Abdullah, M.M.A.B.; Bloch, K.; Nabiałek, M.; Baltatu, M.S.; Sandu, A.V.; Vizureanu, P. Near-Infrared (NIR) Silver Sulfide (Ag₂S) Semiconductor Photocatalyst Film for Degradation of Methylene Blue Solution. *Materials* **2023**, *16*, 437. <https://doi.org/10.3390/ma16010437>

Academic Editor: Juan M. Coronado

Received: 26 November 2022

Revised: 24 December 2022

Accepted: 27 December 2022

Published: 3 January 2023



Copyright: © 2023 by the authors. Licensee MDPI, Basel, Switzerland. This article is an open access article distributed under the terms and conditions of the Creative Commons Attribution (CC BY) license (<https://creativecommons.org/licenses/by/4.0/>).

1. Introduction

Since the prehistoric age, humans have used dyes from natural resources for coloring purposes. The lengthy process, poor colorfastness, excessive cost of producing natural dyes, and the increasing demand for textiles led to the discovery of synthetic dyes from petroleum compounds that outperformed the properties of natural dyes [1–3]. Statistically, more than 7 × 10⁵ tons of synthetic dyes are produced worldwide, and about 1 × 10⁴ of them are used in industry [4]. However, these synthetic dyes have a negative impact on the environment, such as water pollution. Textile industries discharge around 35% of dye wastewater into water bodies as effluent annually [5]. These dyes can contaminate the aquatic habitat,

which may enter the food chain [6,7]. Methylene blue (MB), or $C_{16}H_{18}N_3SCl$, is one of the synthetic dye materials used in textile industries. When dissolved in water, it results in the formation of a blue-colored solution. The discharging of MB dye into the environment is considered as a significant threat for aesthetical and toxicological reasons. In terms of aquatic life, its existence in the water could reduce sunlight transmittance and decrease oxygen solubility due to the high molar absorption coefficient ($\sim 8.4 \times 10^4 \text{ L} \cdot \text{mol}^{-1} \cdot \text{cm}^{-1}$ at 664 nm) of MB dyes [8–10]. At a certain concentration, it can cause serious threats to human health, including respiratory distress, abdominal disorders, blindness, and digestive and mental disorders [11].

In recent years, tremendous attempts have been made to improve industrial wastewater treatment methods. These methods can be divided into physical [12–16], biological [17–21], and chemical methods. For the chemical methods, there are several conventional chemical dye-removal processes that have been used, e.g., the coagulant flocculation, electrochemical destruction, advanced oxidation process (AOP), etc. [22–25]. Amongst these, the advanced oxidation processes (AOPs) have received the most attention due to their significant competence in acting toward a wide range of organic or inorganic dye pollutants in the aqueous phase, by converting those pollutants into stable inorganic compounds such as water, carbon dioxide, and salt without any footprint and sludge production [26,27]. The AOPs also rely on the in situ production of greatly reactive hydroxyl radicals (OH^\bullet) [28].

In the midst of the AOPs, heterogeneous photocatalysis has been considered a leading method and desired breakthrough to cope with organic contaminants. Photocatalysis is a reaction that involves light (photoreaction) and accelerates the reaction due to the presence of a catalyst that absorbs light energy to form the reducing and oxidizing (electron–hole pairs) ions on the surface of the catalyst. The electron's handover occurs during the oxidation–reduction process [29]. The reduction of an acceptor occurs when the electrons (e^-) combine with oxygen in the water to generate an anion (O_2^-), which oxidizes the hydroxyl radical (OH^\bullet), while the hole (h^+) will oxidize the dissolved hydroxyl and convert it into a radical with great energy [30]. These processes work simultaneously. The photocatalytic properties of various metal oxides (e.g., titania, TiO_2 , and zinc oxide, ZnO) have been extensively studied. The results of these studies show that the metal oxides become active potential photocatalysts in wastewater treatment [31–34]. However, due to a wide bandgap, they can only absorb the ultraviolet (UV) light and show poor performance in the visible–near-infrared (NIR) range of the solar spectrum [29,35–37]. In addition, the solar spectrum itself is dominated by the visible (46%) and NIR spectral (49%) rather than the UV spectral (5%) [38]. In addition, the manufacturing cost is relatively high for many of the metal oxide materials [39,40]. Therefore, metal sulfides have become an option.

Among all of the metal sulfide photocatalyst materials, silver sulfide (Ag_2S) shows more efficient charge separation, attributed to the remarkable synergistic effects of strong NIR light absorption and excellent surface properties [41,42]. Furthermore, compared to the other metal sulfide compounds such as cadmium selenide, CdS , and lead selenide, PbS , Ag_2S is found to be acceptable for wastewater treatment due to its non-toxic properties [43–45]. Silver sulfide has an eminent performance in the degradation of pollutants, solar energy conversion, and production of hydrogen with various approaches that have been well established for synthesizing a variety of visible–NIR-light driven Ag_2S photocatalysts. For example, Ag_2S synthesized using the facile ion-exchange method at room temperature can be used as an effective photocatalyst for the decomposition of methylene orange (MO). The results of a study confirmed the excellent photo-oxidation performance of Ag_2S since MO can be completely photodegraded with Ag_2S in just 30 min, and 70 min under visible light and NIR light irradiation. This performance is due to the narrow band gap of Ag_2S , 1.078 eV, and the lower recombination efficiency and photogenerated electron–hole pairs of Ag_2S during the photocatalytic process [46]. The Ag_2S photocatalyst has usually been used in the powder form [43,47–49]. This is because the photocatalyst powder can be well dispersed in suspensions [50].

However, this photocatalyst powder exhibits certain drawbacks especially for nano-sized powders/particles. During the degradation process, the photocatalyst may undergo coagulation due to the instability of the nano-sized particles, which will hamper the light incidence on the active centers, consequently reducing its catalytic activity [51]. Furthermore, for the slurry system, the main challenge is to recover the nano-sized photocatalyst particles from the treated water [52–54]. This condition leads to the requirements of high filtration costs of catalyst removal [55], hindering its industrial application and impractical. In addition, the Ag₂S nanoparticles are susceptible to photo-corrosion, which means that the sulfide ions have the potential to be oxidized into sulfur by photogenerated holes when they are exposed to irradiation [56]. There have been a lot of efforts towards increasing the photocatalytic efficiency and preventing the photo-corrosion of Ag₂S [57–60]. A photocatalyst film is one of the plausible material technologies to diminish the impacts of photocatalyst powder on the environment [61]. A photocatalyst film has promising performance in terms of adsorption and efficient mass transport. The adsorption ability is maxed out by the larger surface area that allows more catalyst deposit in the film, resulting in higher photocatalytic activity. Moreover, the mass transport of reactants, intermediates, and products is enhanced by the compact substrate that allows better contact with the catalyst, and prevents the leakage of the powder of the photocatalyst material into clean water [62,63]. Table 1 shows the cost comparison for some types of photocatalyst, especially titania (TiO₂), which is a common photocatalyst used for industrial purposes. Those types of photocatalyst are used under a UV lamp-assisted reactor for the photocatalytic processes and consume a certain amount of energy (power). For an industrial batch process, it will consume a lot of energy with a higher cost of operation. Thus, our study introduces a composite film (cellulose/Ag₂S) that can effectively degrade methylene blue concentrations using only sunlight, which is cost-effective. Furthermore, the composite film can also be easily removed from the water after the treatment process without a costly separation method.

Table 1. Comparison of the cost-effectiveness assessment of several photocatalysts.

Type of Photocatalyst	Types of Wastewater	Energy Sources	Catalyst Dosage (g/L)	Maximum Photodegradation Efficiency	Time to Obtain Maximum Photodegradation (min.)	Total Power Consumed (kWh)	Operational Cost (USD/kg) ^b	Refs.
Rutile TiO ₂	Acetaldehyde	UV lamps (56 W)	5.01	80	100	not available	127.13	[64]
GAC ^a -TiO ₂	Livestock wastewater	UV lamps (56 W)	6	100	6	0.524	0.68	[65]
V ₂ O ₅ -TiO ₂	Methylene blue	UV lamps	4.75	92	120	1	8.7205	[66]
TiO ₂ /O ₃	Tert-butyl alcohol	UVA lamps (15W)	not available	75	10	37	not available	[67]
Cellulose/Ag ₂ S	Methylene blue	Solar energy	7	100	120	0	0	Current study

^a Granular activated carbon. ^b Energy costs (USD) per kg of wastewater removal.

To date, bio-based products such as cellulose film have become attractive compounds due to their excellent properties that are harmless to the environment. A cellulose film has distinctive characteristics such as transparency, robustness, low water content, etc. These properties lead to the wide usage of cellulose film as a renewable alternative to petroleum-based materials [68]. Furthermore, it is hypothesized that cellulose may become one of the solutions to improve the efficiency of electron donors and to establish the hole (h^+) transporter during the light irradiation process. To the best of our knowledge, the incorporation of Ag_2S powder into cellulose film has not been studied, although the integration between semiconductor catalyst and cellulose film is a promising innovation for photocatalytic applications. Therefore, the integration of Ag_2S in cellulose-derived film is hoped to enhance the photocatalytic efficiency. Thus, this study aimed to synthesize cellulose/ Ag_2S film in the presence of an alkali/urea solution using a simple solution casting method to describe the transformation of the functional group and the structure of the cellulose thin film due to the deposition of Ag_2S . We also compared the photocatalytic efficiency of the commercial Ag_2S and synthesized Ag_2S doped into the cellulose film via the degradation of the MB solution.

2. Materials and Methods

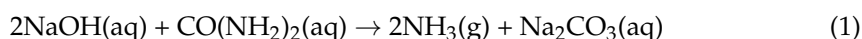
The current study successfully synthesized films that were stated as CFs for cellulose film, cellulose films with commercial Ag_2S (CF/com Ag_2S), and cellulose films with synthesized Ag_2S (CF/synt Ag_2S). The materials and methods used for synthesizing the Ag_2S photocatalyst film are described in the section below.

2.1. Materials and Reagents

The materials and reagents used consist of microcrystalline cellulose, MCC ($\leq 100\%$), commercial silver sulfide, Ag_2S , silver nitrate, AgNO_3 , thiourea, $(\text{NH}_2)_2\text{CS}$, and polyvinyl alcohol, PVA. All of these materials were bought from Sigma-Aldrich. The PVA was dissolved with distilled water at the temperature of 90°C until the transparent PVA solution with a concentration of 5.0% (w/w) occurred. Chemicals including sodium hydroxide (NaOH), glycerol ($\text{C}_3\text{H}_8\text{O}_3$), and acetone ($\text{C}_3\text{H}_6\text{O}$) were supplied by HmbG chemicals. The acetone was diluted in distilled water with a ratio of 2:1 as the agent of regeneration for cellulose films, called an acetone bath. Urea ($\text{CO}(\text{NH}_2)_2$) was obtained from Bendosen Laboratory Chemicals.

2.2. Preparation of Sodium Hydroxide/Urea (NaOH /urea) Aqueous Solution

To obtain the NaOH /urea solution, the NaOH pellets and urea powder were weighed to obtain 7 g and 12 g of mass, respectively [47,69]. Subsequently, each sample of NaOH and urea was diluted in a separate beaker glass before being mixed in a 100 mL volumetric flask. The balanced chemical reaction worked in the mixture can be written as:



The solution was agitated to obtain a homogenous solution. Once the homogeneity was obtained, the solution was stored for the next process.

2.3. Liquid Phase Rarefaction of Commercial Ag_2S by Magnetic Stirring Technique

Prior to the incorporation of the commercial Ag_2S into the cellulose film, it was essential to break down the bulk Ag_2S into smaller particle sizes. In this step, the commercial Ag_2S powder was weighed according to the mass variation that is displayed in Table 2.

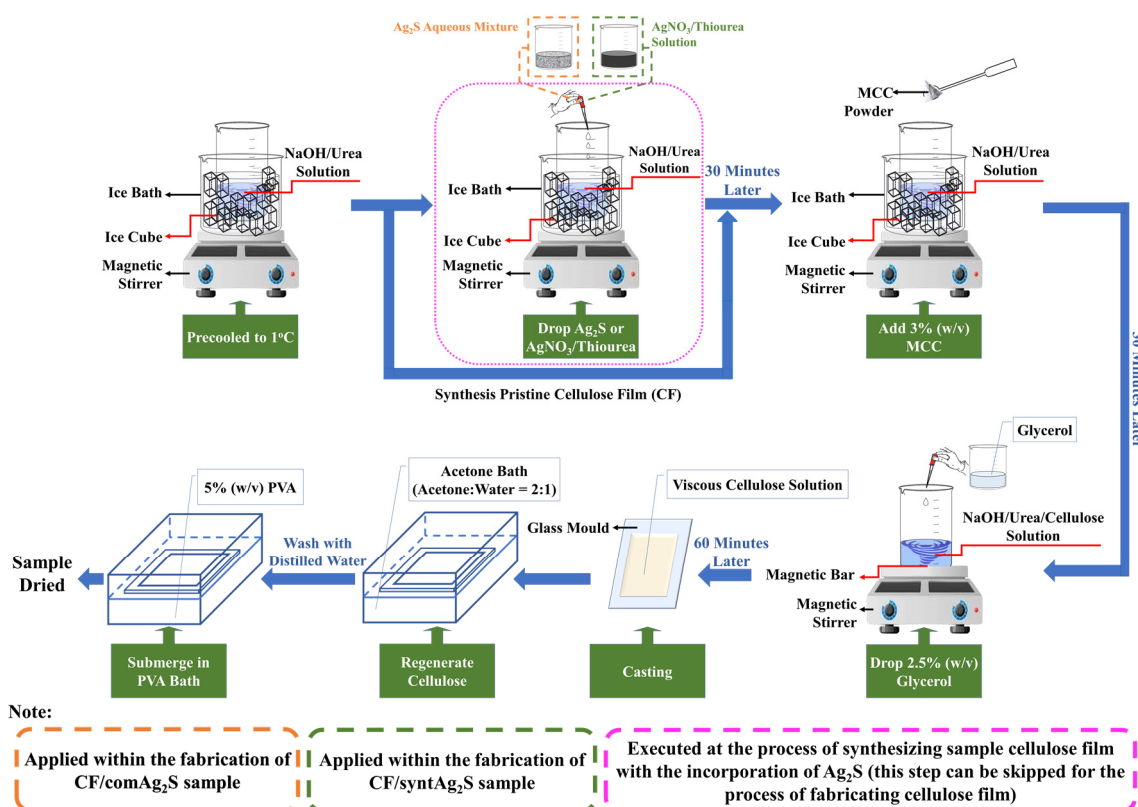
Table 2. Sample code and composition of refracted commercial Ag₂S.

Sample Code	Ag ₂ S Mass (Gram)	Volume of Distilled Water (mL)
CF/comAg ₂ S1	0.075	6.0
CF/comAg ₂ S2	0.100	6.0
CF/comAg ₂ S3	0.300	6.0

After the desired amount of Ag₂S was obtained, the powder was placed into a beaker containing 6 mL of distilled water and vigorously stirred using a magnetic stirrer under ambient temperature for 24 h. The crystallite size of rarefaction Ag₂S was then investigated using X-ray diffraction (XRD) to confirm its size reduction.

2.4. Synthesis of the Cellulose Film

The cellulose films were prepared using a solution casting method. The cellulose with NaOH/urea aqueous solution was used as the main reagent to synthesize the cellulose films. Both commercial Ag₂S and synthesized Ag₂S were incorporated into the cellulose system to study the different behavior of the cellulose film with commercial and synthesized Ag₂S. The composition of NaOH, urea, and water was different for each process as shown in Table 3. Figure 1 shows the overall schematic procedure to synthesize the CFs, CF/comAg₂S, and CF/syntAg₂S samples.

**Figure 1.** Schematic illustration of sequence process to synthesize the samples.

2.4.1. Synthesis Cellulose Film (CF) and Cellulose Film/Commercial Ag₂S (CF/comAg₂S)

At the beginning of the process, 15 mL of NaOH/urea aqueous solution was pre-cooled to a temperature of ~1 °C in the ice bath. After that, 3 wt% of microcrystalline cellulose (MCC) was added into the pre-cooled solvent, and the mixture was rapidly agitated for 20 min. Then, the cellulose solution was taken out from the ice bath and 2.5 wt% of glycerol [70] was wisely dropped into the solution. Afterwards, the solution was spun for

another hour to achieve the homogeneity. Once the dope and viscous solution was obtained, it was cast onto an 8.5 cm × 6 cm × 0.2 cm glass mold. Subsequently, the casted sample was regenerated in an acetone coagulant bath [71] until opaque-sheet-like cellulose hydrogel was formed. The hydrogel was soaked in distilled water for neutralization. Before drying, the hydrogel was submerged in a 5 wt% polyvinyl alcohol (PVA) bath for 2 h [72]. Finally, a transparent cellulose film was obtained. The same steps were also conducted in order to synthesize the CF/comAg₂S specimens, except the 6 mL of refracted Ag₂S produced from Section 2.3 was first poured into the NaOH/urea solution prior to the addition of the desired amount of MCC into the precooled solution.

2.4.2. Synthesis of Cellulose Film/Synthesized Ag₂S (CF/syntAg₂S)

The co-precipitation method was used to synthesize the Ag₂S particles. Silver nitrate and thiourea were the main precursors to produce the Ag₂S slurry. The presence of silver and sulfide ions in the solution was required for the chemical deposition process to occur in order to complete the formation of Ag₂S. The chemical reaction involved during the deposition process is shown in the following formulas [73,74]:

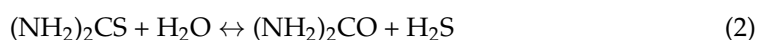


Table 3 shows the final composition that was utilized in this section for the whole synthesis process:

Table 3. Sample code and sample composition to synthesize samples CF/syntAg₂S.

Sample Code	Molarity of AgNO ₃	AgNO ₃ Solution		Thiourea Solution			
		AgNO ₃	Water	NaOH	Thiourea	Urea	Water
CF/syntAg ₂ S1	0.1 M	0.084 g	5.0 mL	1.6 g	1.3 g	1.6 g	10.5 mL
CF/syntAg ₂ S2	0.3 M	0.254 g	5.0 mL	1.6 g	1.3 g	1.6 g	10.5 mL
CF/syntAg ₂ S3	0.5 M	0.422 g	5.0 mL	1.6 g	1.3 g	1.6 g	10.5 mL

According to Table 3, the total volume of solution that was used in the synthesis of CF/syntAg₂S samples was 20 mL (5 mL AgNO₃ solution and 15 mL thiourea solution). The solutions were prepared in two different beakers. At the beginning of the process, 15 mL of thiourea solution was poured into a 50 mL glass beaker while stirring on a magnetic stirrer. After that, the 5 mL of AgNO₃ solution was added dropwise into the stirred thiourea solution. At this stage, a black precipitate was obtained, which indicated the formation of Ag₂S particles. The solution was left to stir for another 15 min to ensure all of the substances completely reacted. Then, the precipitated solution was precooled in the ice bath for 20 min. Subsequently, 3% *w/v* of MCC powder was added into the black cold-precipitated solution and continuously stirred until the MCC was well dispersed in the solution. The mixed solution was then removed from the ice bath, dripped with glycerol, and spun for an entire hour. The cellulose/synthesized AgNO₃ solution was transferred into the glass mold and then regenerated by using an acetone bath and PVA bath, in sequence. Lastly, the cellulose film obtained after the regenerated film was open-air dried for 2 days. All of the procedures above were repeated for different molarities of synthesized AgNO₃.

2.5. Photocatalytic Activity Test

For photocatalytic testing, a concentration of 10 ppm of methylene blue (MB) solution was prepared. An amount of 0.1 g of MB powder was diluted with distilled water in a 100 mL volumetric flask. Afterwards, 0.7 g of each sample was submerged into a glass beaker consisting of 70 mL of 10 ppm MB and immediately exposed to sunlight for a total of 300 min. Every 30 min, about 40 mL of the irradiated solution was transferred into a glass vial with a dropper to investigate its degradation behavior using an ultraviolet-visible

(UV-Vis) spectrophotometer, (Lambda 25, Perkin Elmer, Waltham, MA, USA) with 650 nm of wavelength. The degradation ratio of MB was determined using Equation (4); where A_t is the degradation ratio, I_0 is base absorbance, and I_t is absorbency after time t [33,73,75].

$$A_t = \frac{I_0 - I_t}{I_0} \times 100 \quad (4)$$

2.6. Characterizations

To identify chemical bonds and to locate the functional group of the cellulose films, the samples were characterized using a Fourier-transform infrared (FTIR) analysis. The analysis was carried out using an ATR-Perkin Elmer Spectrometer 2000 FT-IR, based on the attenuated total reflection (ATR) approach to ensure non-destructive analysis. The measurement was conducted under 650 cm^{-1} – 4000 cm^{-1} and 4 cm^{-1} resolution. The phase determination and crystallite size measurement were conducted using a Rigaku RINT 2000 X-ray diffraction (XRD). The reflection mode with monochromator-filtered Cu K α radiation ($\lambda = 0.15418\text{ nm}$) at 30 kV and 10 mA was applied. Samples were prepared in two different ways depending on the type of tested sample. For the powder sample, it was loaded onto the XRD sample holder with a small circle cavity in the middle of the holder. For film samples, the cellulose film was cut into a size of 25 mm, thickness $\leq 8\text{ mm}$, and stuck on the holder. The prepared samples were subsequently scanned with 2θ in the range between 15° and 80° . The Debye-Scherrer Equation (5) was generated to compute the crystallite size and the degree of crystallinity was obtained from Equation (6) as follows:

$$D = \frac{K\lambda}{\beta \cos \theta} \quad (5)$$

$$\text{Degree of Crystallinity} = \frac{\text{Area of all crystalline peaks}}{\text{Total area under XRD peaks}} \times 100 \quad (6)$$

where, D = crystallite size (nm); K = Scherrer's constant ($K = 0.94$); λ = the wavelength of X-ray (1.54178 \AA); β = full width half maximum (FWHM); θ = angle of diffraction (rad) [76].

3. Results and Discussion

3.1. The Formation of Cellulose-Photocatalyst Film

In nature, the structure of cellulose includes both axial C–H bonds and equatorial hydroxyl groups. Hence, it has amphiphilic properties with the inter-layer region being hydrophobic and the intra-layer region being hydrophilic. The intra- and intermolecular hydrogen bonds should be broken to a large extent when the cellulose is dissolved in the solvent [77]. Thus, when cellulose is dissolved in the NaOH/urea solution, it is expected that the NaOH interacts with the hydrophilic hydroxyl groups of cellulose, breaking the hydrogen bond between the chains, and the urea reacts with the hydrophobic portions, resulting in a solution that dissolves cellulose [78].

In this study, it was also discovered that the semi-crystalline properties of the cellulose can impact the end-product of the prepared films. During the drying process, the cellulose films will experience severe shrinkage [72,79,80]. Nevertheless, when 2.5% *w/v* glycerol and 5% PVA bath was applied, the shrinkage of the film samples became less. This is because the existence of PVA as a plasticizer in the film can improve the toughness of the cellulose glycerol composite films [73]. The commercial Ag₂S powder was micron- sized and might affect the distribution of particles when incorporated in the MCC film. Thus, the rarefaction process was conducted as shown in Figure 2.

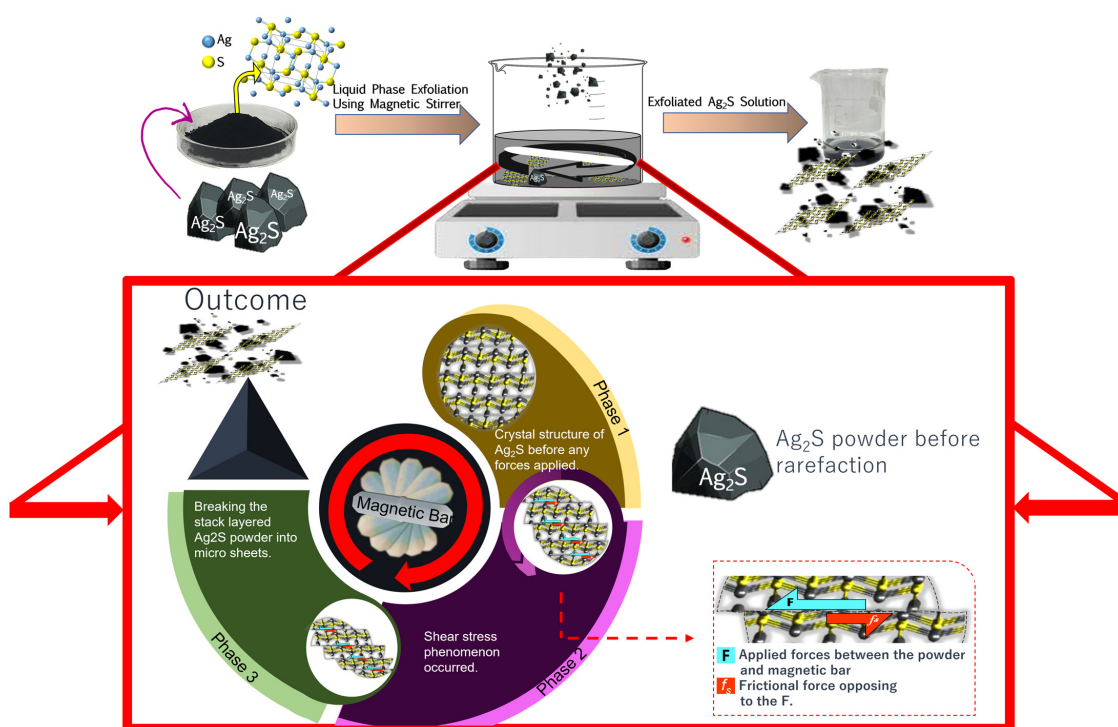


Figure 2. Illustrated scheme of the rarefaction process of commercial semiconductor Ag_2S .

The particle size transformations were involved during the process. The stirring action from the magnetic stirrer was deployed in a clockwise direction at a certain speed in the liquid while applying fluidic shear forces among the involved substances [81]. The existence of opposing forces between the applied forces and the friction forces within the system (Figure 2) caused the occurrence of shear stress in the Ag_2S powders, which can reduce the Ag_2S particle size. The longer the magnetic bar rotates, the more forces work, resulting in more energy provided to wear down the Ag_2S powder. Thus, smaller crystal Ag_2S were formed. According to the peak analysis and crystallite size calculation, it was confirmed that before stirring, the Ag_2S particle has a crystallite size of 52 nm and this size was reduced to 10 nm after the rarefaction process. Thus, the purpose of the rarefaction in this study was succeeded.

The distribution of both the rarefacted and synthesized Ag_2S powder in the cellulose film can be observed in Figure 3. According to Figure 3d–f, the particles from the synthesized Ag_2S particles evenly spread in the whole area of the cellulose matrix. Meanwhile, the samples that were loaded with the commercial Ag_2S had diverse particle distributions (Figure 3a–c). It was shown that part of the cellulose film was not affected by the Ag_2S . The degree of crystallinity and the crystallite size of the synthesized Ag_2S can be categorized as one of the factors that affected this particle distribution. Therefore, further discussion about the structure and chemical function of the samples will be explained in the following section.

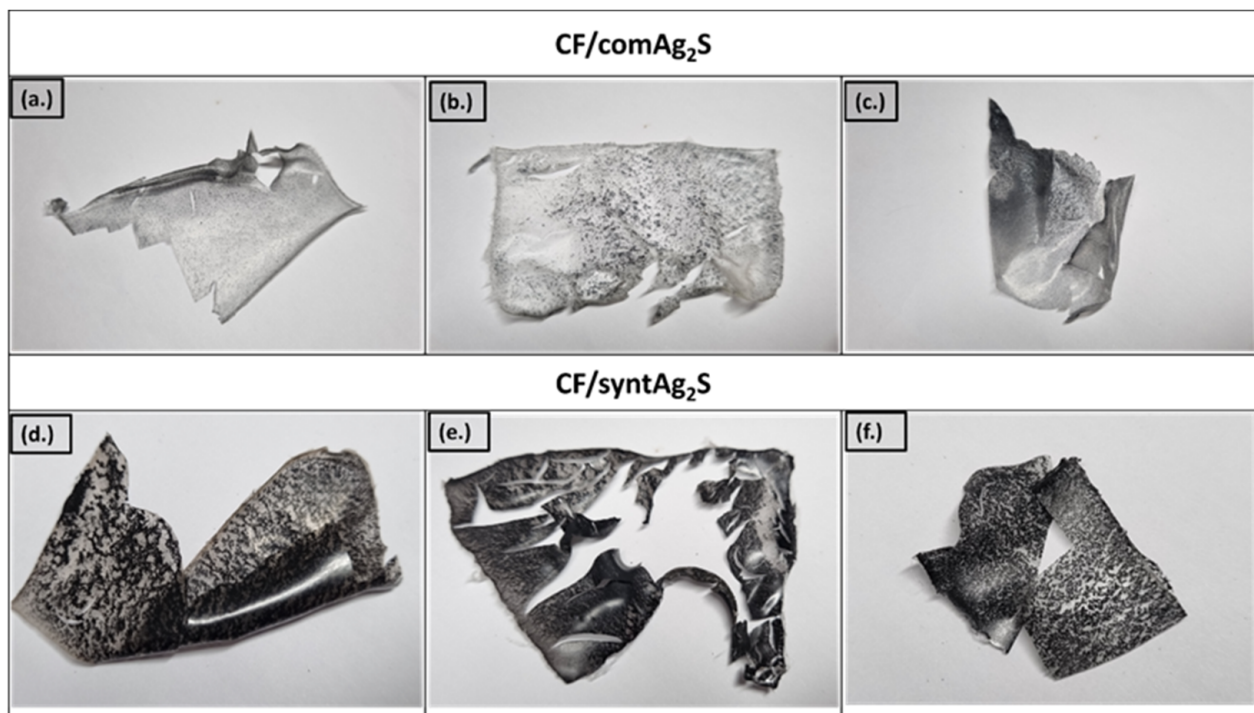


Figure 3. Prepared cellulose films: (a) CF/comAg₂S1, (b) CF/comAg₂S2, (c) CF/comAg₂S3, (d) CF/syntAg₂S1, (e) CF/syntAg₂S2, and (f) CF/syntAg₂S3.

3.2. Crystalline Phase Investigation of the Synthesized Ag₂S powder

Figure 4 shows the XRD spectra of the synthesized Ag₂S particles that were obtained from the reaction of 0.3 M AgNO₃ and thiourea. The diffraction peaks of Ag₂S that were observed at 2θ = 22.4°, 25.9°, 28.9°, 31.5°, 34.4°, 36.8°, 37.7°, 40.7°, 43.6°, and 46.2° showed similar patterns with the commercial Ag₂S and confirmed the formation of Ag₂S phase (ICDD No. 00-014-0072) with monoclinic structure.

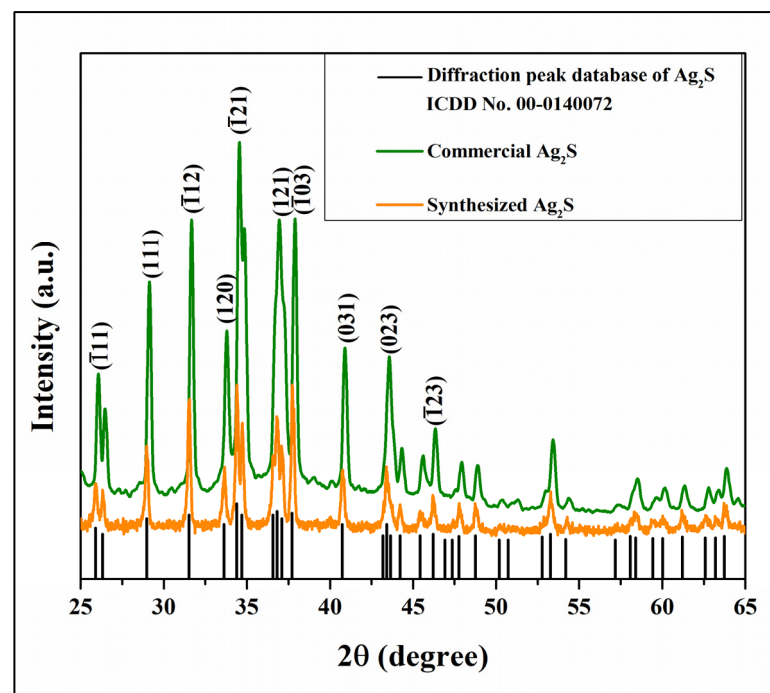


Figure 4. X-ray diffraction spectrum of synthesized Ag₂S.

3.3. Crystal Structure and Phase Identification of Cellulose Film/Synthesized Ag_2S (CF/synt Ag_2S)

To ensure the formation of the synthesized silver sulfide in the cellulose film samples, it was necessary to delve into the characterization of their crystal structure and phase identification. Furthermore, the influence of the AgNO_3 concentration on the crystal structure of the sample was also studied. The crystallite is crucial because the crystallinity of the catalyst in the film will have a direct impact on the photocatalytic properties.

The study of the crystal structure of the CF/synt Ag_2S sample confirmed that all as-prepared samples have diffraction peaks of a monoclinic Acanthine Ag_2S structure with space group P_{21}/C . The specific lattice parameter of these samples can be indexed as $a = 9.5200 \text{ \AA}$, $b = 6.9300 \text{ \AA}$, and $c = 8.2900 \text{ \AA}$. Moreover, the peak of (002) due to the reflection of the cellulose plane also existed in all of the samples that had undergone different AgNO_3 /thiourea loadings during the synthesis. The acquired peaks of the Ag_2S and cellulose were matched well with the references ICDD No. 00-009-0422 and ICDD No. 00-050-2241, respectively. The average grain size and degree of crystallinity of the samples are shown in Table 4.

Table 4. Phase identification and crystallinity of the CF/synt Ag_2S sample.

Sample Code	Index Miller Cellulose				Index Miller Ag ₂ S				Crystallite Size (Å)	Degree of Crystallinity (%)
	(002)		— (3 11)		(220)		(022)			
	2θ Std.	2θ Ob.	2θ Std.	2θ Ob.	2θ Std.	2θ Ob.	2θ Std.	2θ Ob.		
CF/syntAg ₂ S1	22.78	22.76	31.56	-	34.50	34.44	36.92	37.18	221	47.93
CF/syntAg ₂ S2	22.78	22.30	31.56	31.18	34.50	33.99	36.92	36.47	188	76.76
CF/syntAg ₂ S3	22.78	22.78	31.56	31.48	34.50	34.49	36.92	36.99	174	37.75

In terms of peak intensity, it was observed that the higher the concentration, the lower and broader the peak (see Figure 5), which is attributed to the low crystallite size of the sample [82]. Table 4 illustrates that the smallest yield of crystallite size was found from the highest concentration of the substituent (CF/synt Ag_2S). Furthermore, Table 4 also depicts that the substituent was responsible for the shifted peak that occurred in the sample with concentrated loadings. The shifted peak towards the lower 2theta indicated that the lattice parameter of the pristine cellulose had been incorporated by the synthesized Ag_2S [83,84].

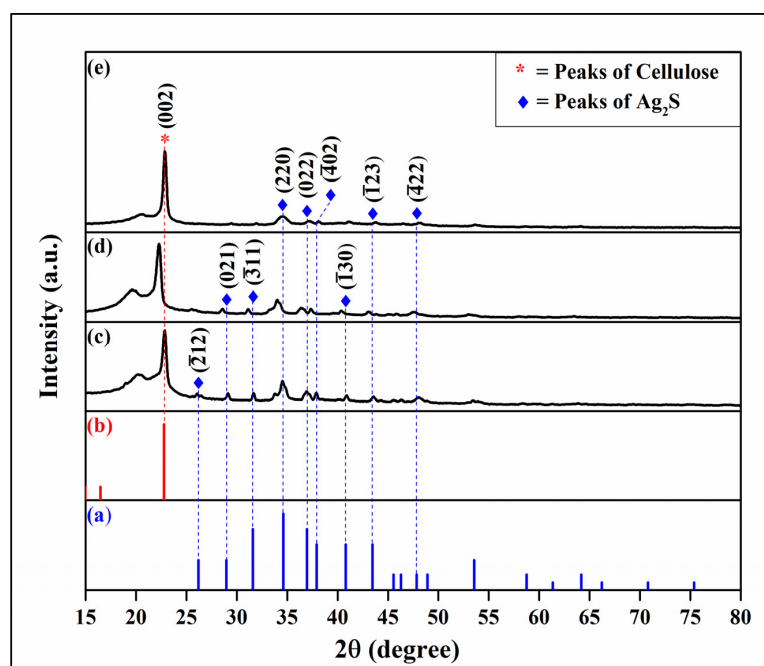


Figure 5. X-ray diffraction spectra of: (a) database of Ag_2S (ICDD No. 00-009-0422), (b) database of cellulose (ICDD No. 00-050-2241), (c) CF/synt Ag_2S 1, (d) CF/synt Ag_2S 2, and (e) CF/synt Ag_2S 3.

3.4. Functional Group Analysis of CF/comAg₂S and CF/syntAg₂S

According to Figure 6, the commercial (Figure 6a–d) and synthesized (Figure 6g–j) samples had comparable FTIR patterns along the observation scanning range. However, in terms of peak intensity, the sample with the synthesized Ag₂S had a sharp and narrow peak compared to the commercial sample. The spectra illustrated the same pattern among the thin films that were either impregnated by the commercial or synthesized Ag₂S. The broad bands that were found from wavenumber 3336.5 cm^{−1} to 3419.8 cm^{−1} were designated to the hydroxyl (O–H) group stretching vibration. The shifted peak among these bands was attributed to the interaction of the hydrogen bond of the pristine cellulose with glycerol and PVA. These displacements were also found by [71,85], in which the high content of glycerol and PVA in the cellulose matrix impacted the sharpening and shifting to the higher wavenumber. The spectral band located from 2916.5 cm^{−1} to 2912.59 cm^{−1}, as well as a weak peak at 897.00 cm^{−1} were attributed to the characteristic of symmetrical stretching of C–H from the alkyl group [32] and glycosidic CH deformation [72], respectively.

Thereafter, the transmittance band at the area of 1753.70 cm^{−1} to 1752.13 cm^{−1} was associated with the stretching vibration of the C=O ester carbonyl group and the medium peak at the range of 1238 cm^{−1} was denoted as C–O–C asymmetric stretching [86]. The authentic peak of cellulose was found at the region around 1059 cm^{−1} and remarked as C–O–C stretching vibrations of aliphatic primary and secondary alcohols in cellulose [87,88]. The peak of C–H bending was observed at the regions of 1374 cm^{−1} to 1373 cm^{−1}. The study by Cazón et al. announced that the chemical content of glycerol and PVA in the cellulose matrix may contribute to the displacement of the observed peak. Nevertheless, Figure 6e,f,k,l indicates that the loadings of metal silver sulfide into the cellulose can reduce the intensity of the peak with an oxygen-containing functional group. The more concentrated the Ag₂S, the lower the intensity of the peak-contained oxygen functional group. According to Kumar et al., it was confirmed that the strong electrostatic linkages between Ag₂S and the functional groups of cellulose were responsible for the lower intensity of the transmittance peak into the oxygen-containing functional group [89]. This means that the different intensity of the peak, particularly in the range of oxygen-containing group regions, was a characteristic that showed the success of Ag₂S deposited into the cellulose matrix.

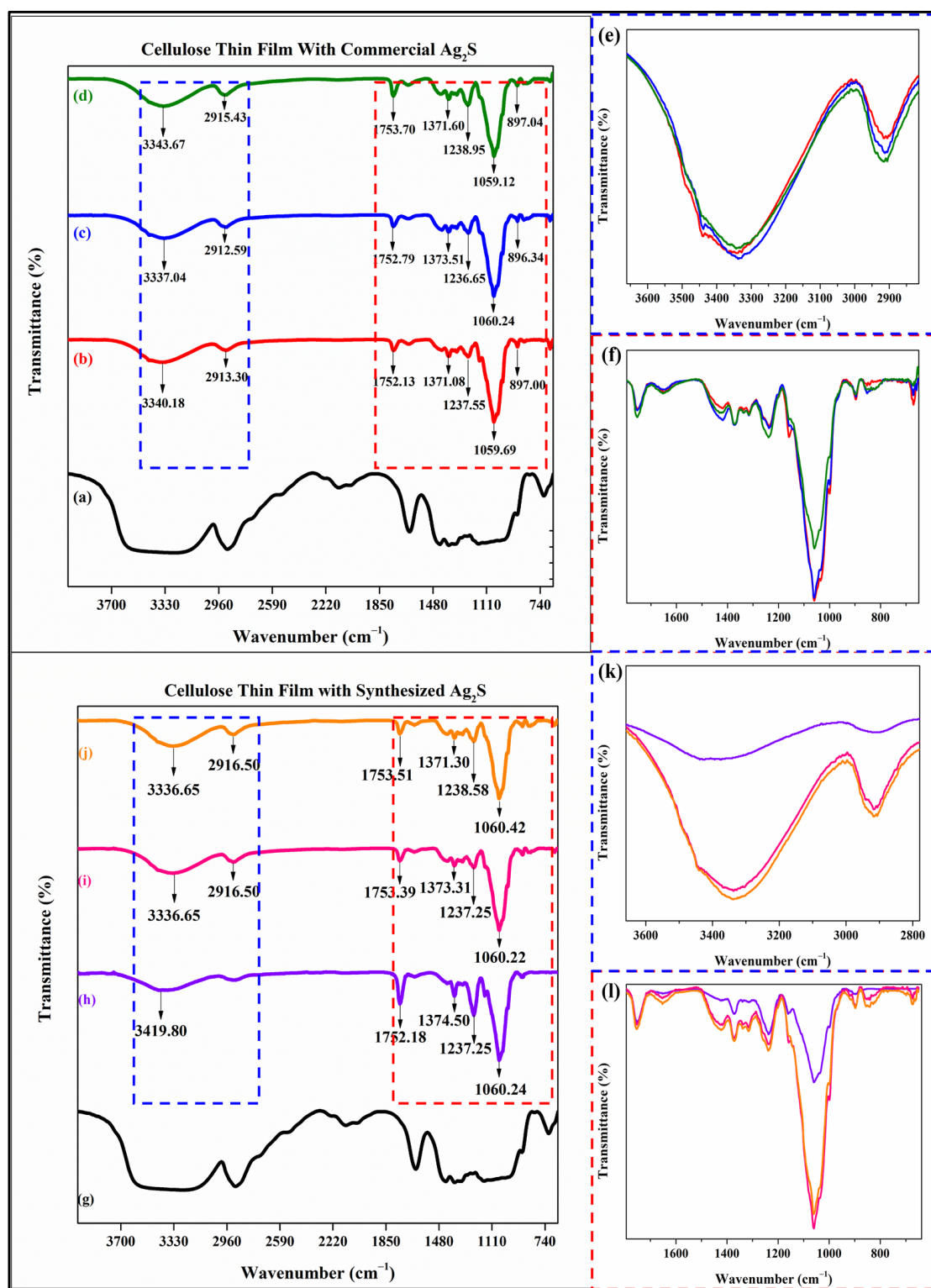


Figure 6. ATR—FTIR spectra of: (a,g) cellulose, (b) CF/com Ag_2S 1, (c) CF/com Ag_2S 2, (d) CF/com Ag_2S 3, (e,f) inset CF/com Ag_2S graph, (h) CF/synt Ag_2S 1, (i) CF/synt Ag_2S 2, (j) CF/synt Ag_2S 3, and (k,l) inset CF/synt Ag_2S graph.

3.5. Photocatalytic Degradation Mechanism of Methylene Blue Using the Cellulose/ Ag_2S Films

The degradation of the methylene blue (MB) dye solution with sunlight exposure and without exposure was investigated. The results are shown in Table 5. For the non-exposure samples, the degradation rate of both synthesized and commercial Ag_2S incorporated

in the cellulose film was only 35% and 33% (due to the adsorption by cellulose film), respectively, even after 5 h of processing. Compared to the same samples that were exposed to sunlight, the degradation rate of MB reached 98–100% within 2 h. This result showed that solar energy seemed to have a great influence on the photocatalytic activity of the Ag₂S-containing samples, since this semiconductor catalyst absorbed in the NIR region. Nevertheless, according to the direct observation of photocatalytic activity under sunlight exposure, there were two kinds of reactions that might have occurred: firstly, the reaction between the cellulose surface and the MB solution; secondly, the reaction among deposited Ag₂S in the cellulose film and the MB solution. Figure 7 shows the reaction mechanism that might have occurred between the cellulose and MB solution during the process.

Table 5. Comparison of the photocatalytic efficiency of the prepared samples.

Exposure Time (Min)	Degradation Ratio (%)					
	Non-Exposure		Ag ₂ S Powder	Pristine Cellulose	With Exposure	
	CF/comAg ₂ S	CF/syntAg ₂ S			CF/comAg ₂ S2	CF/syntAg ₂ S1
0	0	0	0	0	0	0
5	3.59	0.66	19.78	44.14	30.99	31.49
10	5.97	1.60	23.37	53.09	40.77	44.42
15	7.84	3.09	26.85	63.43	52.10	71.71
20	10.44	4.31	30.22	71.10	58.56	83.54
25	12.21	5.64	32.82	75.91	64.92	86.69
30	14.42	6.46	34.53	81.66	69.78	89.45
60	22.76	12.43	39.39	90.88	98.95	93.98
90	27.40	16.24	45.41	94.92	99.01	97.29
120	29.78	21.60	48.18	96.19	100	98.56
150	31.33	25.03	52.98	99.56	100	99.78
180	31.93	28.18	54.92	99.56	100	99.78
210	32.32	30.17	59.28	99.83	100	100
240	32.49	33.81	62.49	99.97	100	100
270	32.71	34.75	66.74	100	100	100
300	33.04	35.08	75.03	100	100	100

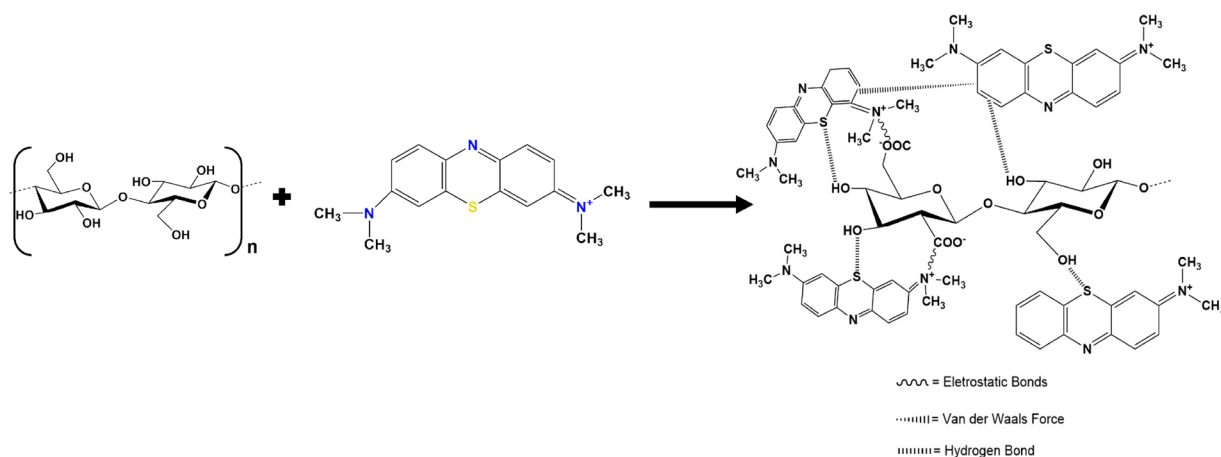
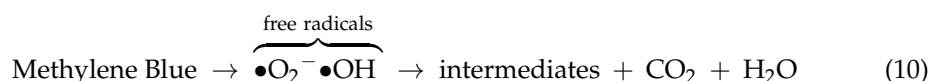


Figure 7. Predicted mechanism reaction between methylene blue and cellulose.

The cellulose interacts with MB through several bonds, such as the electrostatic bond between the ion N⁺ in MB and ion O[−] in cellulose. The electrostatic attraction that was involved in the adsorption mechanism of MB on cellulose led to the enhancement of the MB molecules to quickly fill the adsorption sites on the surface of the cellulose film, resulting in a high rate of MB adsorption [90]. The Van der Waals force (C=C) and hydrogen bond also formed during this process [91]. These bonds made it possible for the cellulose to experience the photolysis reaction when exposed to the solar source.

On the other hand, under solar illumination, the existence of the catalyst Ag₂S in the cellulose film established the photocatalytic activity due to the configuration of the reducing

and oxidizing (electron–hole pairs) ions on the surface of the catalyst, which may degrade the concentration of the MB dyes solution until it reached 100% discoloration (see Table 5). During the process of solar irradiation, photons of solar light with an energy that was either equal to or higher than the band gap of Ag₂S (~1.06 eV) [92] were degraded by Ag₂S. Upon the process of photon absorption, an electron (*e*[−]) from the valence band (VB) was stimulated up to the conduction band (CB). In addition, it was linked to the development of a hole (*h*⁺) in the valence band, which led to the formation of electron–hole pairs that took part in the process of reduction and oxidation. In this process, the electrons in the surface reacted with the oxygen (O₂) that was dissolved in the aqueous solution, which then resulted in the production of anionic superoxide radicals (•O₂[−]) [93]. Simultaneously, the photogenerated holes also reacted with water to create hydroxyl radicals, which further oxidized the dye molecules. The produced anionic superoxide radicals (•O₂[−]) and hydroxyl radicals oxidized the dye molecules that can decompose the MB dyes into CO₂ or H₂O and their intermediates [94]. Overall, this phenomenon can be expressed through the following chemical reactions:



However, without light energy, the processes involving reduction–oxidation reactions in the photocatalysis process will not be formed. As a result, the MB dyes wastewater will only interact with the cellulose film as described above.

The incorporation of Ag₂S into cellulose films served primarily to increase the rate of dye degradation by creating a massive contact surface. The catalyst, Ag₂S, was distributed well toward the cellulose films, leading to the films outperforming the powder counterparts in terms of activity because they effectively absorbed light and perhaps underwent internal scattering within the cellulose/Ag₂S film, inducing higher charge carrier formation and hence better photocatalytic efficiency. Table 5 shows the photocatalytic efficiency for all samples based on the MB degradation rate (%). From the table, when Ag₂S powder was used, the degradation rate of MB only reached about 75% even after 5 h of sunlight exposure. For pristine cellulose, the degradation of MB reached 100% after 4 h exposure. The high rate of MB adsorption by pristine cellulose might be due to the electrostatic attraction that was involved in the adsorption mechanism of the MB molecules to quickly fill the adsorption sites on the surface of the cellulose [90]. For CF/com Ag₂S, 100% of the MB was degraded in 2 h of exposure time compared to the CF/syntAg₂S sample with 98.6% degradation. The deterioration in the treatment that applied the catalyst was compared to the degradation in the photolysis experiment that was also conducted without the presence of a catalyst in the aqueous solution of methylene blue. By observing the direct photolysis of MB, it was clear that there were no appreciable color changes over the 5 h of exposure time. The degradation rate also reached its lowest value, ranging from 0% to 1.66%, as shown in Figure 8a,c.

Based on Figure 8b,d, the concentration of the dye solution was elevated to more than 90% in just 60 min for the pristine cellulose, CF/comAg₂S and CF/syntAg₂S samples, while for the Ag₂S powder, less than 40% of the MB was degraded. This showed that the distribution of Ag₂S powders in regenerated cellulose matrices can enhance the photocatalytic activity up to 100% efficiency due to higher surface area, and the affinity of the photocatalyst films that react with the dye molecules during the sunlight irradiation [95].

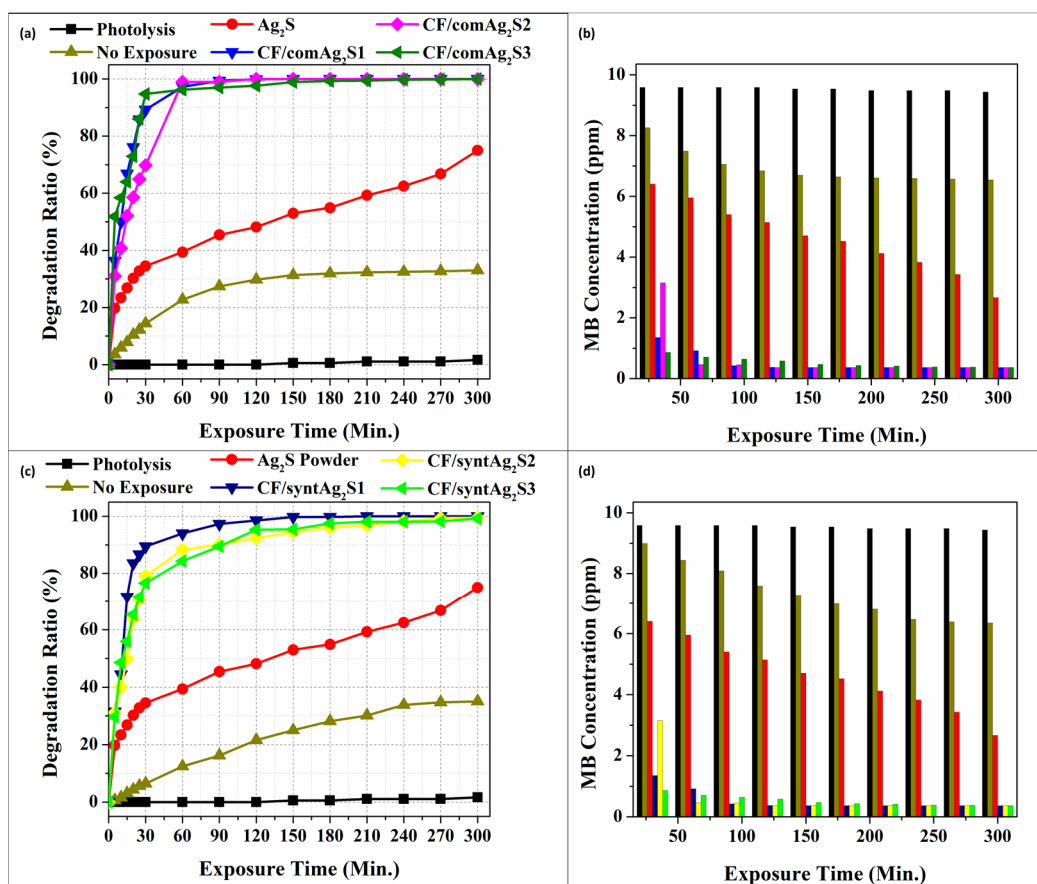


Figure 8. (a) Degradation ratio of MB with Ag₂S commercial as a catalyst; (b) The concentration of MB after photocatalytic activity using CF/comAg₂S samples; (c) Degradation ratio of MB with synthesized Ag₂S as a catalyst; (d) The concentration of MB after photocatalytic activity employing CF/syntAg₂S samples.

In addition, the surface of the cellulose film acted as a host during the process of dye adsorption, which in turn enabled the donor and acceptor molecules to interact with one another. This process could delay the recombination of charge carriers under direct sunlight. Charge recombination must be avoided during this process since it can bring down the efficiency of the photocatalyst [96–98]. In terms of the degradation ratio, it can be seen that there were differences in the photodegradation characterization of the two types of samples that were synthesized. The samples with commercial Ag₂S doping will have an increasing ability with increasing Ag₂S loading, where the higher content that can be accepted by cellulose film is 0.1 g. Meanwhile, the other types of samples (CF/syntAg₂S) showed the opposite nature. This may occur due to overload on the sample (Figure 3d–f) with loading that might exceed the limit, resulting in poor interfacial charge carrier migration and an increase in the recombination rate of photoexcited electron–hole pairs due to an increase in the concentration of Ag sources [73,74]. Thus, it was found that the CF/comAg₂S samples had the efficiency to degrade 100% of the MB content compared to the CF/syntAg₂S (98.6%) in 2 h.

4. Conclusions

It has been successfully demonstrated that silver sulfide (Ag₂S) particles, which were incorporated into regenerated cellulose, outperformed its properties in the powder state. This was because the distribution of Ag₂S particles on the cellulose matrix could increase its photocatalytic activity as the contact surface between the catalyst and dyes became larger. Furthermore, the molecules contained in the cellulose were found to have the

ability to interact with molecules in the dyes, especially the methylene blue (MB) dyes. The samples with the commercial Ag₂S showed an increase in photocatalytic activity up to 100% degradation after 120 min of sunlight exposure with the maximum of 0.1 g Ag₂S loading onto the cellulose film, while other types of samples (CF/syntAg₂S) showed 98.6%. This situation might be due to the overload of synthesized Ag₂S particles on the sample that exceeded the photocatalyst limit on the film. As a result, poor interfacial charge carrier migration and an increase in the recombination rate of photoexcited electron–hole pairs occurred. Thus, it can be concluded that the photocatalytic efficiency of the photocatalyst film originating from the commercial Ag₂S particles was the highest, with 100% of the degradation rates in 2 h. For the non-exposure sunlight samples, the degradation rates were only 33–35%, showing the importance of the NIR semiconductor Ag₂S catalyst used.

Author Contributions: Conceptualization, Z.R.M., N.M. and M.N.N.; methodology, I.S.M., M.M.A.B.A. and K.B.; software, A.V.S.; validation, Z.R.M., N.M. and P.V.; formal analysis, M.N.N.; investigation, I.S.M., M.M.A.B.A. and K.B.; data curation, K.B., M.N. and M.S.B.; writing—original draft preparation, Z.R.M., N.M., M.N.N. and I.S.M.; writing—review and editing, K.B., M.N. and A.V.S.; visualization, M.M.A.B.A.; supervision, P.V.; project administration, M.M.A.B.A.; funding acquisition, M.S.B. All authors have read and agreed to the published version of the manuscript.

Funding: This work was financially supported by the Fundamental Research Grant Scheme FRGS/1/2021/TK0/UNIMAP/02/33 from the Ministry of Education Malaysia (MOE) and by Gheorghe Asachi Technical University of Iasi—TUIASI Romania, Scientific Research Funds, FCSU-2022.

Conflicts of Interest: The authors declare that they have no known competing financial interest or personal relationships that could have appeared to influence the work reported in this paper.

References

1. Ziarani, G.M.; Moradi, R.; Lashgari, N.; Kruger, H.G. Introduction and Importance of Synthetic Organic Dyes. In *Metal-Free Synthetic Organic Dyes*; Elsevier: Amsterdam, The Netherlands, 2018; pp. 1–7. ISBN 978-0-12-815647-6.
2. Fleck, B.; Cabral, I.; Souto, A.P. Eco Printing of Linen and Tencel Substrates with Onion Skins and Red Cabbage. *Mater. Circ. Econ.* **2022**, *4*, 2. [\[CrossRef\]](#)
3. Kusumastuti, A.; Anis, S.; Fardhyanti, D.S. Production of natural dyes powder based on chemo-physical technology for textile application. *IOP Conf. Ser. Earth Environ. Sci.* **2019**, *258*, 012028. [\[CrossRef\]](#)
4. Elshahida, K.; Fauzi, A.M.; Sailah, I.; Siregar, I.Z. Sustainability of the use of natural dyes in the textile industry. *IOP Conf. Ser. Earth Environ. Sci.* **2019**, *399*, 012065. [\[CrossRef\]](#)
5. Hasan, K.M.F.; Wang, H.; Mahmud, S.; Islam, A.; Habib, M.A.; Genyang, C. Enhancing mechanical and antibacterial performances of organic cotton materials with greenly synthesized colored silver nanoparticles. *IJCST*, 2022; *ahead-of-print*. [\[CrossRef\]](#)
6. Bahuguna, A.; Singh, S.; Bahuguna, A.; Sharma, S.; Dadarwal, B. Physical method of Wastewater treatment-A review. *J. Res. Environ. Earth Sci.* **2021**, *7*, 2348–2532.
7. Berradi, M.; Hsissou, R.; Khudhair, M.; Assouag, M.; Cherkaoui, O.; El Bachiri, A.; El Harfi, A. Textile finishing dyes and their impact on aquatic environs. *Heliyon* **2019**, *5*, e02711. [\[CrossRef\]](#)
8. Kosswattaarachchi, A.M.; Cook, T.R. Repurposing the Industrial Dye Methylene Blue as an Active Component for Redox Flow Batteries. *ChemElectroChem* **2018**, *5*, 3437–3442. [\[CrossRef\]](#)
9. Lawagon, C.P.; Amon, R.E.C. Magnetic rice husk ash “cleanser” as efficient methylene blue adsorbent. *Environ. Eng. Res.* **2019**, *25*, 685–692. [\[CrossRef\]](#)
10. Zhou, M.; Chen, J.; Hou, C.; Liu, Y.; Xu, S.; Yao, C.; Li, Z. Organic-free synthesis of porous CdS sheets with controlled windows size on bacterial cellulose for photocatalytic degradation and H₂ production. *Appl. Surf. Sci.* **2019**, *470*, 908–916. [\[CrossRef\]](#)
11. Wang, H.; Li, G.; Fakhri, A. Fabrication and structural of the Ag₂S-MgO/graphene oxide nanocomposites with high photocatalysis and antimicrobial activities. *J. Photochem. Photobiol. B Biol.* **2020**, *207*, 111882. [\[CrossRef\]](#)
12. Hammood, Z.A.; Chyad, T.F.; Al-Saedi, R. Adsorption Performance of Dyes Over Zeolite for Textile Wastewater Treatment. *Ecol. Chem. Eng. S* **2021**, *28*, 329–337. [\[CrossRef\]](#)
13. Januário, E.F.D.; Vidovix, T.B.; Calsavara, M.A.; Bergamasco, R.; Vieira, A.M.S. Membrane surface functionalization by the deposition of polyvinyl alcohol and graphene oxide for dyes removal and treatment of a simulated wastewater. *Chem. Eng. Process.—Process Intensif.* **2022**, *170*, 108725. [\[CrossRef\]](#)
14. Khan, M.M.; Pradhan, D.; Sohn, Y. (Eds.) Nanocomposites for Visible Light-induced Photocatalysis. In *Springer Series on Polymer and Composite Materials*; Springer International Publishing: Cham, Germany, 2017; ISBN 978-3-319-62445-7.
15. Popa, N.; Visa, M. New hydrothermal charcoal TiO₂ composite for sustainable treatment of wastewater with dyes and cadmium cations load. *Mater. Chem. Phys.* **2021**, *258*, 123927. [\[CrossRef\]](#)

16. Singh, R.; Munya, V.; Are, V.N.; Nayak, D.; Chattopadhyay, S. A Biocompatible, pH-Sensitive, and Magnetically Separable Superparamagnetic Hydrogel Nanocomposite as an Efficient Platform for the Removal of Cationic Dyes in Wastewater Treatment. *ACS Omega* **2021**, *6*, 23139–23154. [\[CrossRef\]](#)
17. Azimi, B.; Abdollahzadeh-Sharghi, E.; Bonakdarpour, B. Anaerobic-aerobic processes for the treatment of textile dyeing wastewater containing three commercial reactive azo dyes: Effect of number of stages and bioreactor type. *Chin. J. Chem. Eng.* **2021**, *39*, 228–239. [\[CrossRef\]](#)
18. Haddad, M.; Abid, S.; Hamdi, M.; Bouallagui, H. Reduction of adsorbed dyes content in the discharged sludge coming from an industrial textile wastewater treatment plant using aerobic activated sludge process. *J. Environ. Manag.* **2018**, *223*, 936–946. [\[CrossRef\]](#)
19. Idris, I.; Rahmadhani, I.; Sudiana, I.M. Feasibility of *Aspergillus keratitidis* InaCC1016 for synthetic dyes removal in dyes wastewater treatment. *IOP Conf. Ser. Earth Environ. Sci.* **2020**, *439*, 012027. [\[CrossRef\]](#)
20. Ikram, M.; Zahoor, M.; El-Saber Batiha, G. Biodegradation and decolorization of textile dyes by bacterial strains: A biological approach for wastewater treatment. *Z. Für Phys. Chem.* **2021**, *235*, 1381–1393. [\[CrossRef\]](#)
21. Shen, L.; Jin, Z.; Xu, W.; Jiang, X.; Shen, Y.; Wang, Y.; Lu, Y. Enhanced Treatment of Anionic and Cationic Dyes in Wastewater through Live Bacteria Encapsulation Using Graphene Hydrogel. *Ind. Eng. Chem. Res.* **2019**, *58*, 7817–7824. [\[CrossRef\]](#)
22. Ben Ayed, S.; Azam, M.; Al-Resayes, S.I.; Ayari, F.; Rizzo, L. Cationic Dye Degradation and Real Textile Wastewater Treatment by Heterogeneous Photo-Fenton, Using a Novel Natural Catalyst. *Catalysts* **2021**, *11*, 1358. [\[CrossRef\]](#)
23. Dong, Y.-Y.; Zhu, Y.-H.; Ma, M.-G.; Liu, Q.; He, W.-Q. Synthesis and characterization of Ag@AgCl-reinforced cellulose composites with enhanced antibacterial and photocatalytic degradation properties. *Sci. Rep.* **2021**, *11*, 3366. [\[CrossRef\]](#)
24. Hussin, N.A.M.; Abidin, C.Z.A.; Fahmi; Ibrahim, A.H.; Ahmad, R.; Singa, P.K. Optimization of Anthraquinone Dye Wastewater Treatment using Ozone in the Presence of Persulfate Ion in a Semi-batch Reactor. *IOP Conf. Ser. Earth Environ. Sci.* **2021**, *920*, 012019. [\[CrossRef\]](#)
25. Saeed, M.; Adeel, S.; Muneer, M.; ul Haq, A. Photo Catalysis: An Effective Tool for Treatment of Dyes Contaminated Wastewater. In *Bioremediation and Biotechnology*, Vol 2; Bhat, R.A., Hakeem, K.R., Dervash, M.A., Eds.; Springer International Publishing: Cham, Germany, 2020; pp. 175–187. ISBN 978-3-030-40332-4.
26. Brienza, M.; Katsoyiannis, I. Sulfate Radical Technologies as Tertiary Treatment for the Removal of Emerging Contaminants from Wastewater. *Sustainability* **2017**, *9*, 1604. [\[CrossRef\]](#)
27. Crini, G.; Lichtfouse, E. Advantages and disadvantages of techniques used for wastewater treatment. *Environ. Chem. Lett.* **2019**, *17*, 145–155. [\[CrossRef\]](#)
28. Sengupta, S.; Pal, C.K. Chemistry in Wastewater Treatment. In *Advanced Materials and Technologies for Wastewater Treatment*; CRC Press: Boca Raton, FL, USA, 2021; ISBN 978-1-00-313830-3.
29. Riente, P.; Noël, T. Application of metal oxide semiconductors in light-driven organic transformations. *Catal. Sci. Technol.* **2019**, *9*, 5186–5232. [\[CrossRef\]](#)
30. Gisbertz, S.; Pieber, B. Heterogeneous Photocatalysis in Organic Synthesis. *ChemPhotoChem* **2020**, *4*, 456–475. [\[CrossRef\]](#)
31. Al-Mayyahi, A.; Al-Asadi, A.A. Advanced oxidation processes (aops) for wastewater treatment and reuse: A brief review. *Asian J. Appl. Sci. Technol.* **2018**, *2*, 13.
32. Kumar, N.; Mittal, H.; Reddy, L.; Nair, P.; Ngila, J.C.; Parashar, V. Morphogenesis of ZnO nanostructures: Role of acetate (COOH[−]) and nitrate (NO₃[−]) ligand donors from zinc salt precursors in synthesis and morphology dependent photocatalytic properties. *RSC Adv.* **2015**, *5*, 38801–38809. [\[CrossRef\]](#)
33. Zailan, S.N.; Bouaissi, A.; Mahmed, N.; Abdullah, M.M.A.B. Influence of ZnO Nanoparticles on Mechanical Properties and Photocatalytic Activity of Self-cleaning ZnO-Based Geopolymer Paste. *J. Inorg. Organomet. Polym.* **2020**, *30*, 2007–2016. [\[CrossRef\]](#)
34. Subramaniam, M.N.; Goh, P.-S.; Lau, W.-J.; Ng, B.-C.; Ismail, A.F. Chapter 3—development of nanomaterial-based photocatalytic membrane for organic pollutants removal. In *Advanced Nanomaterials for Membrane Synthesis and its Applications*; Lau, W.-J., Ismail, A.F., Isloor, A., Al-Ahmed, A., Eds.; Micro and Nano Technologies; Elsevier: Amsterdam, The Netherlands, 2019; pp. 45–67. ISBN 978-0-12-814503-6.
35. Ishchenko, O.M.; Rogé, V.; Lamblin, G.; Lenoble, D. TiO₂- and ZnO-based materials for photocatalysis: Material properties, device architecture and emerging concepts. In *Semiconductor Photocatalysis—Materials, Mechanisms and Applications*; Cao, W., Ed.; InTech: London, UK, 2016; ISBN 978-953-51-2484-9.
36. Kanakillam, S.S.; Krishnan, B.; Guzman, S.S.; Martinez, J.A.A.; Avellaneda, D.A.; Shaji, S. Defects rich nanostructured black zinc oxide formed by nanosecond pulsed laser irradiation in liquid. *Appl. Surf. Sci.* **2021**, *567*, 150858. [\[CrossRef\]](#)
37. Haoounati, R.; El Guerdaoui, A.; Ouachtak, H.; El Haouti, R.; Bouddouch, A.; Hafid, N.; Bakiz, B.; Santos, D.M.F.; Labd Taha, M.; Jada, A.; et al. Design of direct Z-scheme superb magnetic nanocomposite photocatalyst Fe₃O₄/Ag₃PO₄@Sep for hazardous dye degradation. *Sep. Purif. Technol.* **2021**, *277*, 119399. [\[CrossRef\]](#)
38. Hu, X.; Li, Y.; Tian, J.; Yang, H.; Cui, H. Highly efficient full solar spectrum (UV-vis-NIR) photocatalytic performance of Ag₂S quantum dot/TiO₂ nanobelt heterostructures. *J. Ind. Eng. Chem.* **2017**, *45*, 189–196. [\[CrossRef\]](#)
39. Dias, P.; Mendes, A. Hydrogen Production from Photoelectrochemical Water Splitting. In *Encyclopedia of Sustainability Science and Technology*; Meyers, R.A., Ed.; Springer: New York, NY, USA, 2018; pp. 1–52. ISBN 978-1-4939-2493-6.
40. Danish, M.S.S.; Bhattacharya, A.; Stepanova, D.; Mikhaylov, A.; Grilli, M.L.; Khosravy, M.; Senjyu, T. A Systematic Review of Metal Oxide Applications for Energy and Environmental Sustainability. *Metals* **2020**, *10*, 1604. [\[CrossRef\]](#)

41. Sadovnikov, S.I.; Gusev, A.I. Recent progress in nanostructured silver sulfide: From synthesis and nonstoichiometry to properties. *J. Mater. Chem. A* **2017**, *5*, 17676–17704. [\[CrossRef\]](#)
42. Shafi, A.; Ahmad, N.; Sultana, S.; Sabir, S.; Khan, M.Z. Ag₂S-sensitized NiO–ZnO heterostructures with enhanced visible light photocatalytic activity and acetone sensing property. *ACS Omega* **2019**, *4*, 12905–12918. [\[CrossRef\]](#)
43. Yu, W.; Yin, J.; Li, Y.; Lai, B.; Jiang, T.; Li, Y.; Liu, H.; Liu, J.; Zhao, C.; Singh, S.C.; et al. Ag₂S Quantum Dots as an Infrared Excited Photocatalyst for Hydrogen Production. *ACS Appl. Energy Mater.* **2019**, *2*, 2751–2759. [\[CrossRef\]](#)
44. Badawi, A. Effect of the non-toxic Ag₂S quantum dots size on their optical properties for environment-friendly applications. *Phys. E Low-Dimens. Syst. Nanostructures* **2019**, *109*, 107–113. [\[CrossRef\]](#)
45. Shahri, N.N.M.; Taha, H.; Hamid, M.H.S.A.; Kusri, E.; Lim, J.-W.; Hobley, J.; Usman, A. Antimicrobial activity of silver sulfide quantum dots functionalized with highly conjugated Schiff bases in a one-step synthesis. *RSC Adv.* **2022**, *12*, 3136–3146. [\[CrossRef\]](#)
46. Jiang, W.; Wu, Z.; Yue, X.; Yuan, S.; Lu, H.; Liang, B. Photocatalytic performance of Ag₂S under irradiation with visible and near-infrared light and its mechanism of degradation. *RSC Adv.* **2015**, *5*, 24064–24071. [\[CrossRef\]](#)
47. Yuan, L.; Lu, S.; Yang, F.; Wang, Y.; Jia, Y.; Kadhim, M.; Yu, Y.; Zhang, Y.; Zhao, Y. A facile room-temperature synthesis of three-dimensional coral-like Ag₂S nanostructure with enhanced photocatalytic activity. *J. Mater. Sci.* **2019**, *54*, 3174–3186. [\[CrossRef\]](#)
48. Al-Shehri, B.M.; Shkir, M.; Bawazeer, T.M.; AlFaify, S.; Hamdy, M.S. A rapid microwave synthesis of Ag₂S nanoparticles and their photocatalytic performance under UV and visible light illumination for water treatment applications. *Phys. E Low-Dimens. Syst. Nanostructures* **2020**, *121*, 114060. [\[CrossRef\]](#)
49. Cui, C.; Li, X.; Liu, J.; Hou, Y.; Zhao, Y.; Zhong, G. Synthesis and Functions of Ag₂S Nanostructures. *Nanoscale Res. Lett.* **2015**, *10*, 431. [\[CrossRef\]](#) [\[PubMed\]](#)
50. Khan, M.M. Metal oxide powder photocatalysts. In *Multifunctional Photocatalytic Materials for Energy*; Elsevier: Amsterdam, The Netherlands, 2018; pp. 5–18. ISBN 978-0-08-101977-1.
51. Nalajala, N.; Patra, K.K.; Bharad, P.A.; Gopinath, C.S. Why the thin film form of a photocatalyst is better than the particulate form for direct solar-to-hydrogen conversion: A poor man's approach. *RSC Adv.* **2019**, *9*, 6094–6100. [\[CrossRef\]](#) [\[PubMed\]](#)
52. Garusinghe, U.M.; Raghuwanshi, V.S.; Batchelor, W.; Garnier, G. Water Resistant Cellulose—Titanium Dioxide Composites for Photocatalysis. *Sci. Rep.* **2018**, *8*, 2306. [\[CrossRef\]](#) [\[PubMed\]](#)
53. Katheresan, V.; Kannedo, J.; Lau, S.Y. Efficiency of various recent wastewater dye removal methods: A review. *J. Environ. Chem. Eng.* **2018**, *6*, 4676–4697. [\[CrossRef\]](#)
54. Samsami, S.; Mohamadizani, M.; Sarrafzadeh, M.-H.; Rene, E.R.; Firoozbahr, M. Recent advances in the treatment of dye-containing wastewater from textile industries: Overview and perspectives. *Process Saf. Environ. Prot.* **2020**, *143*, 138–163. [\[CrossRef\]](#)
55. Wandiga, S.O.; Masese, F.; Mbugua, S.N.; Macharia, J.W.; Otieno, M.A. Challenges and solutions to water problems in Africa. In *Handbook of Water Purity and Quality*; Elsevier: Amsterdam, The Netherlands, 2021; pp. 35–56. ISBN 978-0-12-821057-4.
56. Zhu, C.; Zhang, X.; Zhang, Y.; Li, Y.; Wang, P.; Jia, Y.; Liu, J. Ultrasonic-Assisted Synthesis of CdS/Microcrystalline Cellulose Nanocomposites with Enhanced Visible-Light-Driven Photocatalytic Degradation of MB and the Corresponding Mechanism Study. *Front. Chem.* **2022**, *10*, 892680. [\[CrossRef\]](#)
57. Liu, X.; Sayed, M.; Bie, C.; Cheng, B.; Hu, B.; Yu, J.; Zhang, L. Hollow CdS-based photocatalysts. *J. Mater.* **2021**, *7*, 419–439. [\[CrossRef\]](#)
58. Nawrot, K.C.; Wawrzyńczyk, D.; Bezkrvnyi, O.; Kępiński, L.; Cichy, B.; Samoć, M.; Nyk, M. Functional CdS–Au Nanocomposite for Efficient Photocatalytic, Photosensitizing, and Two-Photon Applications. *Nanomaterials* **2020**, *10*, 715. [\[CrossRef\]](#)
59. Haghighatzadeh, A.; Kiani, M.; Mazinani, B.; Dutta, J. Facile synthesis of ZnS–Ag₂S core–shell nanospheres with enhanced nonlinear refraction. *J. Mater. Sci. Mater. Electron.* **2020**, *31*, 1283–1292. [\[CrossRef\]](#)
60. Zhang, Y.; Zhou, W.; Jia, L.; Tan, X.; Chen, Y.; Huang, Q.; Shao, B.; Yu, T. Visible light driven hydrogen evolution using external and confined CdS: Effect of chitosan on carriers separation. *Appl. Catal. B Environ.* **2020**, *277*, 119152. [\[CrossRef\]](#)
61. Nalajala, N.; Salgaonkar, K.N.; Chauhan, I.; Mekala, S.P.; Gopinath, C.S. Aqueous Methanol to Formaldehyde and Hydrogen on Pd/TiO₂ by Photocatalysis in Direct Sunlight: Structure Dependent Activity of Nano-Pd and Atomic Pt-Coated Counterparts. *ACS Appl. Energy Mater.* **2021**, *4*, 13347–13360. [\[CrossRef\]](#)
62. Thamer, N.H.; Hatem, O.A. Synthesis and Characterization of TiO₂–Ag–Cellulose Nanocomposite and evaluation of photocatalytic degradation efficiency for Congo Red. *IOP Conf. Ser. Earth Environ. Sci.* **2022**, *1029*, 012026. [\[CrossRef\]](#)
63. Mohamed, M.A.; Salleh, W.N.W.; Jaafar, J.; Ismail, A.F.; Mutalib, M.A.; Sani, N.A.A.; Asri, S.E.A.M.; Ong, C.S. Physicochemical characteristic of regenerated cellulose/N-doped TiO₂ nanocomposite membrane fabricated from recycled newspaper with photocatalytic activity under UV and visible light irradiation. *Chem. Eng. J.* **2016**, *284*, 202–215. [\[CrossRef\]](#)
64. Verbruggen, S.; Tytgat, T.; Passel, S.; Martens, J.; Lenaerts, S. Cost-effectiveness analysis to assess commercial TiO₂ photocatalysts for acetaldehyde degradation in air. *Chem. Pap.* **2014**, *68*, 1273–1278. [\[CrossRef\]](#)
65. Asha, R.C.; Vishnuganth, M.A.; Remya, N.; Selvaraju, N.; Kumar, M. Livestock Wastewater Treatment in Batch and Continuous Photocatalytic Systems: Performance and Economic Analyses. *Water Air Soil Pollut.* **2015**, *226*, 132. [\[CrossRef\]](#)
66. Akbarzadeh, R.; Ibrahim, Q.; Jen, T.-C. Photocatalysis and Energy Cost Analysis of Vanadia Titania Thin Films Synthesis. In *Proceedings of the 2019 International Conference on Power Generation Systems and Renewable Energy Technologies (PGSRET)*, Istanbul, Turkey, 26–27 August 2019; pp. 1–3.

67. Mehrjouei, M.; Müller, S.; Möller, D. Catalytic and photocatalytic ozonation of tert-butyl alcohol in water by means of falling film reactor: Kinetic and cost-effectiveness study. *Chem. Eng. J.* **2014**, *248*, 184–190. [\[CrossRef\]](#)
68. Ibrahim, N.A.; Salleh, K.M.; Fudholi, A.; Zakaria, S. Drying Regimes on Regenerated Cellulose Films Characteristics and Properties. *Membranes* **2022**, *12*, 445. [\[CrossRef\]](#)
69. Yang, Q.; Fukuzumi, H.; Saito, T.; Isogai, A.; Zhang, L. Transparent Cellulose Films with High Gas Barrier Properties Fabricated from Aqueous Alkali/Urea Solutions. *Biomacromolecules* **2011**, *12*, 2766–2771. [\[CrossRef\]](#)
70. Cazón, P.; Vázquez, M.; Velazquez, G. Cellulose-glycerol-polyvinyl alcohol composite films for food packaging: Evaluation of water adsorption, mechanical properties, light-barrier properties and transparency. *Carbohydr. Polym.* **2018**, *195*, 432–443. [\[CrossRef\]](#)
71. Geng, H.; Yuan, Z.; Fan, Q.; Dai, X.; Zhao, Y.; Wang, Z.; Qin, M. Characterisation of cellulose films regenerated from acetone/water coagulants. *Carbohydr. Polym.* **2014**, *102*, 438–444. [\[CrossRef\]](#)
72. Cazón, P.; Velazquez, G.; Vázquez, M. Novel composite films from regenerated cellulose-glycerol-polyvinyl alcohol: Mechanical and barrier properties. *Food Hydrocoll.* **2019**, *89*, 481–491. [\[CrossRef\]](#)
73. Holi, A.M.; Zainal, Z.; Ayal, A.K.; Chang, S.-K.; Lim, H.N.; Talib, Z.A.; Yap, C.-C. Ag₂S/ZnO Nanorods Composite Photoelectrode Prepared by Hydrothermal Method: Influence of Growth Temperature. *Optik* **2019**, *184*, 473–479. [\[CrossRef\]](#)
74. Holi, A.M.; Zainal, Z.; Al-Zahrani, A.A.; Ayal, A.K.; Najm, A.S. Effect of Varying AgNO₃ and CS(NH₂)₂ Concentrations on Performance of Ag₂S/ZnO NRs/ITO Photoanode. *Energies* **2022**, *15*, 2950. [\[CrossRef\]](#)
75. Haounati, R.; Alakhras, F.; Ouachtak, H.; Saleh, T.A.; Al-Mazaideh, G.; Alhajri, E.; Jada, A.; Hafid, N.; Addi, A.A. Synthesized of Zeolite@Ag₂O Nanocomposite as Superb Stability Photocatalysis Toward Hazardous Rhodamine B Dye from Water. *Arab. J. Sci. Eng.* **2022**, *207*, 112157. [\[CrossRef\]](#)
76. Hajizadeh, Z.; Taheri-Ledari, R.; Asl, F.R. Identification and analytical methods. In *Heterogeneous Micro and Nanoscale Composites for the Catalysis of Organic Reactions*; Elsevier: Amsterdam, The Netherlands, 2022; pp. 33–51. ISBN 978-0-12-824527-9.
77. Medronho, B.; Romano, A.; Miguel, M.G.; Stigsson, L.; Lindman, B. Rationalizing cellulose (in) solubility: Reviewing basic physicochemical aspects and role of hydrophobic interactions. *Cellulose* **2012**, *19*, 581–587. [\[CrossRef\]](#)
78. Xiong, B.; Zhao, P.; Cai, P.; Zhang, L.; Hu, K.; Cheng, G. NMR spectroscopic studies on the mechanism of cellulose dissolution in alkali solutions. *Cellulose* **2013**, *20*, 613–621. [\[CrossRef\]](#)
79. Mohamed, M.A.; Salleh, W.N.W.; Jaafar, J.; Ismail, A.F.; Abd Mutalib, M.; Jamil, S.M. Incorporation of N-doped TiO₂ nanorods in regenerated cellulose thin films fabricated from recycled newspaper as a green portable photocatalyst. *Carbohydr. Polym.* **2015**, *133*, 429–437. [\[CrossRef\]](#)
80. Zeng, J.; Liu, S.; Cai, J.; Zhang, L. TiO₂ Immobilized in Cellulose Matrix for Photocatalytic Degradation of Phenol under Weak UV Light Irradiation. *J. Phys. Chem. C* **2010**, *114*, 7806–7811. [\[CrossRef\]](#)
81. Desai, J.A.; Adhikari, N.; Kaul, A.B. Chemical exfoliation efficacy of semiconducting WS₂ and its use in an additively manufactured heterostructure graphene-WS₂-graphene photodiode. *RSC Adv.* **2019**, *9*, 25805–25816. [\[CrossRef\]](#)
82. Ma, Y.; Zhao, Z.; Xian, Y.; Wan, H.; Ye, Y.; Chen, L.; Zhou, H.; Chen, J. Highly Dispersed Ag₂S Nanoparticles: In Situ Synthesis, Size Control, and Modification to Mechanical and Tribological Properties towards Nanocomposite Coatings. *Nanomaterials* **2019**, *9*, 1308. [\[CrossRef\]](#)
83. Wang, Q.; Cai, J.; Zhang, L. In situ synthesis of Ag₃PO₄/cellulose nanocomposites with photocatalytic activities under sunlight. *Cellulose* **2014**, *21*, 3371–3382. [\[CrossRef\]](#)
84. Wu, J.; Zhao, N.; Zhang, X.; Xu, J. Cellulose/silver nanoparticles composite microspheres: Eco-friendly synthesis and catalytic application. *Cellulose* **2012**, *19*, 1239–1249. [\[CrossRef\]](#)
85. Rouhi, M.; Razavi, S.H.; Mousavi, S.M. Optimization of crosslinked poly (vinyl alcohol) nanocomposite films for mechanical properties. *Mater. Sci. Eng. C* **2017**, *71*, 1052–1063. [\[CrossRef\]](#) [\[PubMed\]](#)
86. Abderrahim, B.; Abderrahman, E.; Aqil, M. Ouassini Krim Kinetic Thermal Degradation of Cellulose, Polybutylene Succinate and a Green Composite: Comparative Study. *Sci. Educ. Publ.* **2015**, *3*, 95–110. [\[CrossRef\]](#)
87. Dutta, D.; Hazarika, R.; Dutta, P.D.; Goswami, T.; Sengupta, P.; Dutta, D.K. Synthesis of Ag–Ag₂S Janus nanoparticles supported on an environmentally benign cellulose template and their catalytic applications. *RSC Adv.* **2016**, *6*, 85173–85181. [\[CrossRef\]](#)
88. Fujii, Y.; Imagawa, K.; Omura, T.; Suzuki, T.; Minami, H. Preparation of Cellulose/Silver Composite Particles Having a Recyclable Catalytic Property. *ACS Omega* **2020**, *5*, 1919–1926. [\[CrossRef\]](#)
89. Kumar, P.; Agnihotri, R.; Wasewar, K.L.; Uslu, H.; Yoo, C. Status of adsorptive removal of dye from textile industry effluent. *Desalination Water Treat.* **2012**, *50*, 226–244. [\[CrossRef\]](#)
90. Tan, K.B.; Abdullah, A.Z.; Horri, B.A.; Salamatinia, B. Adsorption Mechanism of Microcrystalline Cellulose as Green Adsorbent for the Removal of Cationic Methylene Blue Dye. *J. Chem. Soc. Pak.* **2016**, *38*, 651–664.
91. Manna, S.; Roy, D.; Saha, P.; Gopakumar, D.; Thomas, S. Rapid methylene blue adsorption using modified lignocellulosic materials. *Process Saf. Environ. Prot.* **2017**, *107*, 346–356. [\[CrossRef\]](#)
92. Zamiri, R.; Abbastabar Ahangar, H.; Zakaria, A.; Zamiri, G.; Shabani, M.; Singh, B.; Ferreira, J.M.F. The structural and optical constants of Ag₂S semiconductor nanostructure in the Far-Infrared. *Chem. Cent. J.* **2015**, *9*, 28. [\[CrossRef\]](#)
93. Andrade-Guel, M.; Díaz-Jiménez, L.; Cortés-Hernández, D.; Cabello-Alvarado, C.; Ávila-Orta, C.; Bartolo-Pérez, P.; Gamero-Melo, P. Microwave assisted sol-gel synthesis of titanium dioxide using hydrochloric and acetic acid as catalysts. *Boletín De La Soc. Española De Cerámica Y Vidr.* **2019**, *58*, 171–177. [\[CrossRef\]](#)

94. Isac, L.; Cazan, C.; Enesca, A.; Andronic, L. Copper Sulfide Based Heterojunctions as Photocatalysts for Dyes Photodegradation. *Front. Chem.* **2019**, *7*, 694. [[CrossRef](#)] [[PubMed](#)]
95. Fan, J.; Yu, D.; Wang, W.; Liu, B. The self-assembly and formation mechanism of regenerated cellulose films for photocatalytic degradation of C.I. Reactive Blue 19. *Cellulose* **2019**, *26*, 3955–3972. [[CrossRef](#)]
96. Fan, G.-Z.; Wang, Y.-X.; Song, G.-S.; Yan, J.-T.; Li, J.-F. Preparation of microcrystalline cellulose from rice straw under microwave irradiation. *J. Appl. Polym. Sci.* **2017**, *134*, 44901. [[CrossRef](#)]
97. Ahmaruzzaman, M. Biochar based nanocomposites for photocatalytic degradation of emerging organic pollutants from water and wastewater. *Mater. Res. Bull.* **2021**, *140*, 111262. [[CrossRef](#)]
98. Tavker, N.; Gaur, U.K.; Sharma, M. Agro-waste extracted cellulose supported silver phosphate nanostructures as a green photocatalyst for improved photodegradation of RhB dye and industrial fertilizer effluents. *Nanoscale Adv.* **2020**, *2*, 2870–2884. [[CrossRef](#)]

Disclaimer/Publisher’s Note: The statements, opinions and data contained in all publications are solely those of the individual author(s) and contributor(s) and not of MDPI and/or the editor(s). MDPI and/or the editor(s) disclaim responsibility for any injury to people or property resulting from any ideas, methods, instructions or products referred to in the content.